ACS Energy LETTERS

http://pubs.acs.org/journal/aelccp

# Single-Atom Catalysts with Unsaturated Co−$N_2$ Active Sites Based on a $C_2N$ 2D-Organic Framework for Efficient Sulfur Redox Reaction

Dawei Yang, Jiaao Wang, Chenjie Lou, Mengyao Li, Chaoqi Zhang, Alberto Ramon, Canhuang Li, Mingxue Tang, Graeme Henkelman, Ming Xu,* Junshan Li, Jordi Llorca, Jordi Arbiol, David Mitlin,* Guangmin Zhou,* and Andreu Cabot*

Cite This: *ACS Energy Lett.* 2024, 9, 2083−2091

Read Online

ACCESS | Metrics & More | Article Recommendations | Supporting Information

**ABSTRACT:** The lithium−sulfur battery (LSB) is a viable option for the next generation of energy storage systems. However, the shuttle effect of lithium polysulfides (LiPS) and the poor electrical conductivity of sulfur and lithium sulfides limit its deployment. Here, we report on a 2D-organic framework, $C_2N$, with a high loading of low-coordination cobalt single atoms (Co-SAs/$C_2N$) as an effective sulfur host in LSB cathodes. Experimental and computational results reveal that unsaturated Co−$N_2$ active sites with an asymmetric electron distribution act as effective polysulfide traps, accommodating electrons from polysulfide ions to form strong $S_x^{2-}$−Co−N bonds. Additionally, charge transfer between LiPS and unsaturated Co−$N_2$ active sites endows immobilized LiPS with low free energy and low electrochemical decomposition energy barriers, thus accelerating the kinetic conversion of LiPS. As a result, S@Co-SAs/$C_2N$-based cathodes exhibit superior rate performance, impressive cycling stability, and good areal capacity at high sulfur loading, 2-fold that of commercial lithium-ion batteries. This work emphasizes the potential capabilities and promising prospects of single-atom catalysts with unsaturated coordination in LSBs.

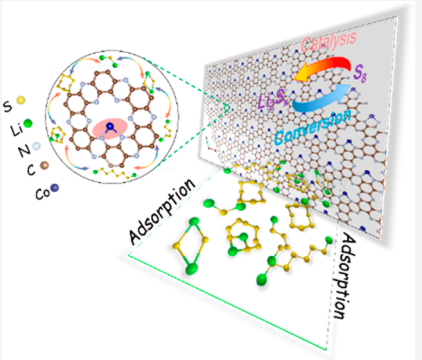


Sulfur has received much attention as a potential cathode material in Li-ion batteries owing to its high theoretical capacity (1672 mAh $g^{-1}$), large energy density (2600 Wh $kg^{-1}$), huge abundance, and low cost.[1−3] However, the commercial deployment of lithium−sulfur batteries (LSBs) has been hampered by several limitations. These limitations include the electrical insulating nature of sulfur and lithium sulfide, which limits the rate capability and reduces the utilization of active material.[4,5] Besides, the lithium polysulfides (LiPS) formed during the electrochemical $S_8$−$Li_2S$ redox reaction are soluble in conventional organic electrolytes and can migrate to the anode.[6,7] Therefore, strategies to promote charge transport at the cathode, immobilize the LiPS, and facilitate their reaction kinetics are highly desired.[6,7]

One effective approach to overcome some of these challenges is to combine sulfur with high surface area and porous carbon-based materials to increase the cathode electrical conductivity and at the same time confine the LiPS.[8−10] However, the weak interaction between nonpolar carbon and polar LiPS prevents fully suppressing their dissolution and migration. On the other hand, some polar inorganic materials showing strong chemical interaction with polysulfides have been proposed to more effectively anchor and confine LiPS.[11−13] However, even when strongly bound to a cathode additive, the sluggish conversion kinetics of adsorbed LiPS results in an accumulation of LiPS that is eventually released into the solution. Thus, in addition to large surface area conductive additives and mechanisms for trapping LiPS, the integration of electrocatalysts that are able to facilitate the LiPS redox reactions is required.

Carbon-supported single-atom catalysts (SACs), offering high activities with almost 100% atomic utilization, are an excellent candidate to overcome the kinetic limitations of the Li−S reaction.[14−17] In addition, some SACs also exhibit high sulfiphilicity, which enables them to contribute to the immobilization of LiPS. The electrocatalytic activity of SACs strongly depends on the metal local environment, which is determined by the local coordination configuration.[18] M−$N_4$

**Received:** March 16, 2024
**Revised:** April 1, 2024
**Accepted:** April 8, 2024

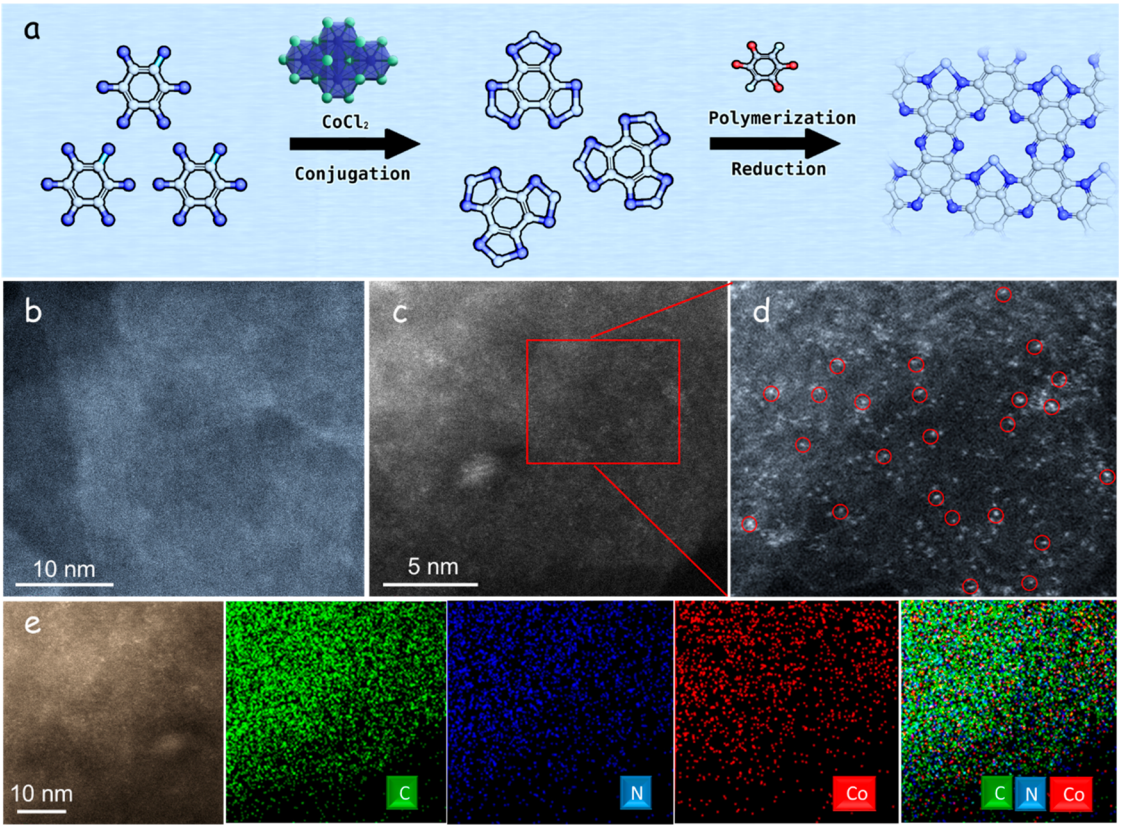


**Figure 1.** (a) Schematic illustration of the synthesis of Co single atoms supported by $C_2N$ (Co-SAs/$C_2N$) (dark blue = nitrogen, light gray = carbon, red = oxygen, light green = chlorine, and light blue = cobalt). (b–d) HAADF-STEM images at different magnifications of Co-SAs/$C_2N$. Red circles display single Co atoms shown as bright contrast spots. (e) HAADF-STEM image and corresponding EDX mapping showing the elemental distribution of Co-SAs/$C_2N$.

moieties (M = Fe, Co, Ni, etc.) are the active sites of the commonly reported SACs.[19−21] SACs with M−$N_4$ moieties afford symmetrical electron distributions, which limit the adsorption and activation of reaction intermediates, thus their catalytic performance.[22,23] Improved performances can be obtained with the asymmetrical electron distribution of M−$N_x$ ($x \neq 4$) coordination structures. While these electrocatalytic moieties have been previously tested,[15] there is a lack of understanding of the relationship between the electronic structure of M−$N_x$ SACs and electrocatalytic performance toward LiPS conversion.

Aside from the metal moiety, the carbon support also influences the electrocatalytic performance. Two-dimensional (2D) carbon supports with a high specific surface area and lamellar structure can accommodate a massive density of SAC active sites. Recently, $C_2N$ has sparked significant interest as a novel graphene-like covalent organic framework characterized by a huge specific surface area and effective charge transfer.[24] $C_2N$ consists of a uniform porous structure with hollow sites surrounded by six pyridine nitrogen atoms ($N_6$ cavities) that provide a large number of effective sites for the coordination of a high density of single metal atoms.[25−27] Within this framework, the diffusion barrier of metal atoms is too high to form aggregates. These properties make $C_2N$ an excellent support for the rational design and engineering of SACs with an asymmetrical electron distribution to improve the electrochemical performance of LSBs.

In this work, we detail the synthesis of dispersed Co single atoms supported on $C_2N$ (Co-SAs/$C_2N$) with a Co−$N_2$ coordination structure through a pyrolysis-free wet-chemistry strategy. The choice of Co to showcase the potential of our approach is related to the numerous previous reports demonstrating the potential of Co-based materials as excellent catalysts for the sulfur redox reaction. The unsaturated Co−$N_2$ sites can not only provide strong LiPS adsorption but also promote interfacial charge transfer to accelerate the redox kinetics of the LiPS. Benefiting from the simultaneous optimization of the carbon support and the SAC's coordination environment, Co-SAs/$C_2N$ exhibits excellent electrocatalytic activity that enables bidirectional sulfur redox chemistry, accelerating the precipitation/decomposition of $Li_2S$ and lowering the related energy barriers. The performance of the S@Co-SAs/$C_2N$ cathodes is thoroughly tested to demonstrate their superior cycling stability and rate capability. The outstanding obtained results are rationalized with the help of density functional theory (DFT) calculations.

A scalable wet-chemistry strategy was designed for the synthesis of $C_2N$-supported Co-based SACs (Figure 1a). Briefly, $Co^{2+}$ was coordinated with nitrogen atoms from hexaaminobenzene (HAB) to form the Co−HAB complex. Subsequently, Co−HAB was polymerized and reduced in the presence of chloranilic acid to form Co-SAs/$C_2N$. The targeted material has a periodic conjugated ring structure with Co ions confined in the $C_2N$ pores. Scanning electron microscopy (SEM) analysis showed Co-SAs/$C_2N$ to display a stacked−layered structure (Figure S1a). According to energy-dispersive X-ray spectroscopy (EDX) results, the N/Co atomic ratio of Co-SAs/$C_2N$ is ca. 2, which corresponds to an average of 1


https://doi.org/10.1021/acsenergylett.4c00771
ACS Energy Lett. 2024, 9, 2083−2091

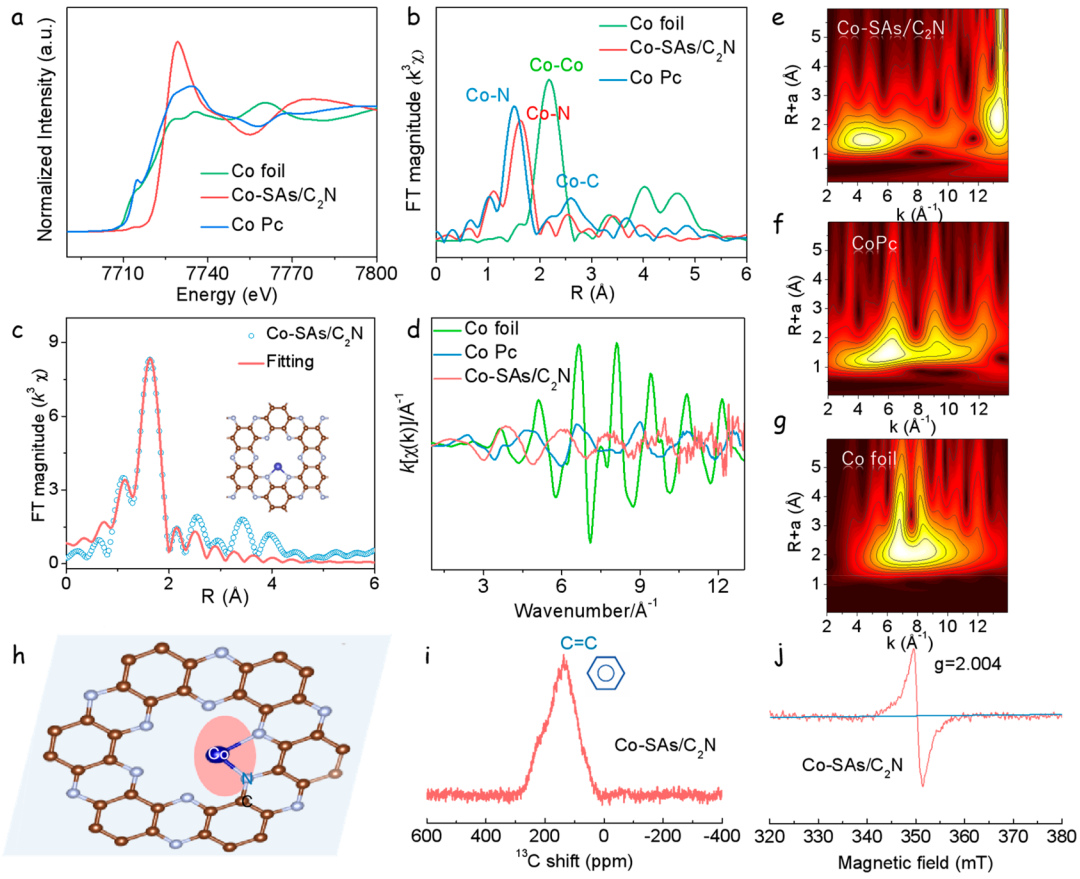


**Figure 2.** (a) XANES spectra and (b) Co K-edge FT-EXAFS spectra in R space of Co-SAs/$C_2N$, CoPc, and Co foil. (c) EXAFS fitting curves in R space for the Co-SAs/$C_2N$ sample. (d) EXAFS oscillations of Co-SAs/$C_2N$ with respect to the reference samples. (e–g) Wavelet transformed contour plots at the Co K-edge of Co-SAs/$C_2N$, CoPc, and Co foil. (h) The atomic structure model of the Co-SAs/$C_2N$. (i) Solid-state $^{13}C$ MAS NMR spectrum for Co-SAs/$C_2N$. (j) CW-EPR spectrum of Co-SAs/$C_2N$.

$Co^{2+}$ ion every 2 N sites in $C_2N$ (Figure S1b). Inductively coupled plasma optical emission spectroscopy (ICP-OES) determined the Co loading in Co-SAs/$C_2N$ to be 12.8% and demonstrated the synthesis to be highly reproducible in terms of the obtained Co loading (Table S1). This high metal loading, above those of generally reported SACs (Table S2), is enabled by the high density of anchoring sites and pores in $C_2N$. Additionally, it is noted that the same method can be used for the synthesis of Ni/$C_2N$ and Fe/$C_2N$ SCAs (Figure S3).

Aberration-corrected high-angle annular dark-field scanning transmission electron microscopy (AC HAADF-STEM) analysis showed no cobalt nanoparticles or clusters anywhere around the Co-SAs/$C_2N$ sample (Figure 1b). In contrast, as highlighted with red circles in Figure 1c,d, a large number of highly dispersed bright spots, identified as Co atoms, were observed within the $C_2N$ skeleton. EDX elemental mapping demonstrated C, N, and Co to be homogeneously distributed within Co-SAs/$C_2N$ (Figure 1e). X-ray diffraction (XRD) patterns of the as-synthesized Co-SAs/$C_2N$ show the characteristic peak of $C_2N$ and no signal related to Co-based compounds (Figures S2 and S3). This result indicates a uniform and atomic dispersion of Co within the $C_2N$ matrix, which is consistent with the AC HAADF-STEM analysis.

X-ray photoelectron spectroscopy (XPS) analysis of Co-SAs/$C_2N$ displays the presence of Co, C, N, and O (Figure S4). The presence of oxygen is related to the exposure of the sample to air before the XPS measurement.[12,28] The high-resolution N 1s XPS spectrum was fitted with four bands at 398.9, 401.2, 402.3, and 399.8 eV, corresponding to pyridinic-N, pyrrolic-N, graphitic-N, and Co–N bonds,[29−31] respectively (Figure S4c). In the Co 2p XPS spectrum (Figure S4d), besides the satellite peaks, a single doublet at 781.3 and 797.5 eV pointed at the existence of Co within a $Co^{2+}$ chemical environment.[9,31]

X-ray absorption near-edge structure (XANES) measurements of the Co K-edge were used to further reveal the chemical structure of Co-SAs/$C_2N$ and particularly the valence state of Co, using cobalt phthalocyanine (CoPc) and Co foil as references (Figure 2a, Table S3). The Co K-edge XANES profile indicates that the Co atoms in Co-SAs/$C_2N$ are at a higher oxidation state than those of CoPc and Co foil, which is compatible with a Co–$N_2$ coordination.[32,33] The absorption edge further indicated that the Co coordination environment is compatible with the Co–$N_2$ bonds within the $C_2N$ structure.

Figure 2b shows the Fourier-transformed extended X-ray absorption fine structure (FT-EXAFS) spectrum of Co-SAs/$C_2N$, which displays a peak at ∼1.62 Å that can be identified as a Co–N scattering path. This result is again compatible with Co atoms being coordinated with N atoms within the $C_2N$ support. Notice also that the Co–Co peak at ∼2.25 Å observed in the Co foil was not observed in the Co-SAs/$C_2N$ spectrum, again suggesting that isolated Co atoms were anchored on the $C_2N$ matrix by Co–N coordination.[34,35]

From the fitting of the EXAFS spectra at the Co K-edge (Figure 2c), the average coordination number of Co atoms


https://doi.org/10.1021/acsenergylett.4c00771
ACS Energy Lett. 2024, 9, 2083−2091

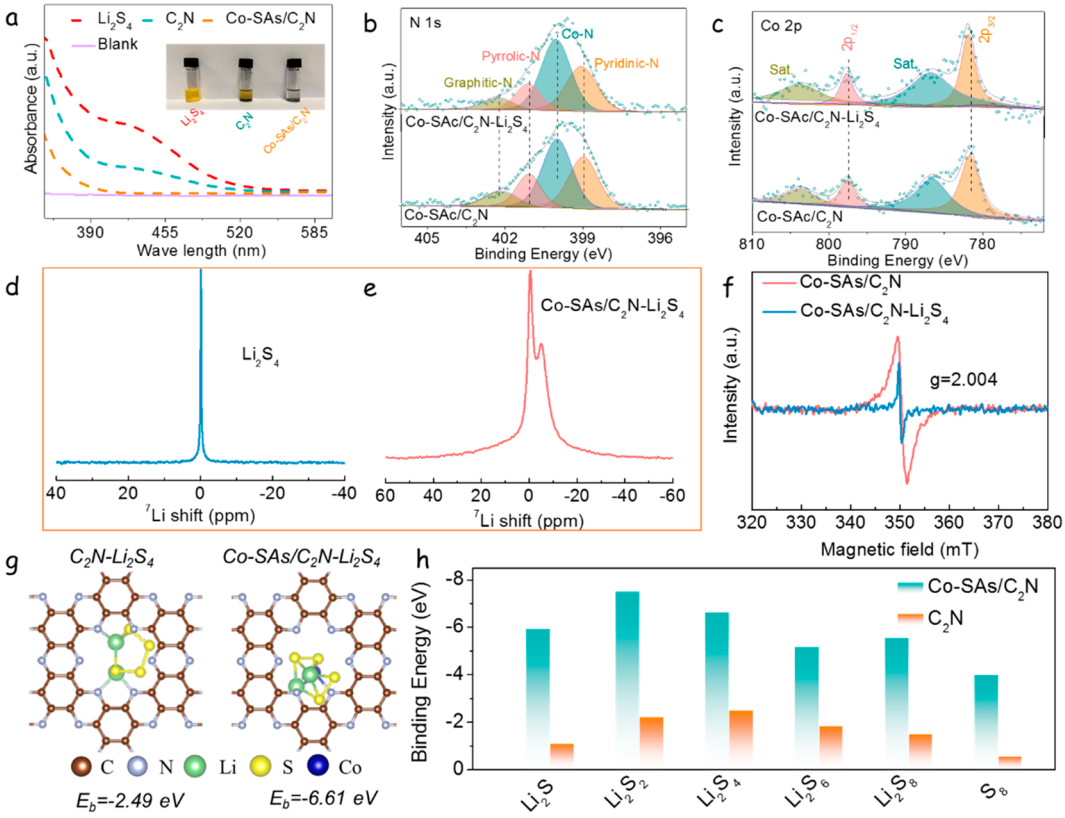


**Figure 3. (a) UV−vis spectra and optical photograph of the flasks containing a $Li_2S_4$ solution and the different materials after overnight adsorption. (b) High-resolution N 1s XPS spectra and (c) Co 2p XPS spectra of Co-SAs/$C_2N$ before and after $Li_2S_4$ adsorption. Solid-state $^7$Li NMR spectrum of (d) $Li_2S_4$ and (e) Co-SAs/$C_2N$−$Li_2S_4$. (f) CW-EPR spectrum for Co-SAs/$C_2N$ and Co-SAs/$C_2N$−$Li_2S_4$. (g) Relaxed $Li_2S_4$-adsorbed structure on the surface of $C_2N$ and Co-SAs/$C_2N$ calculated with DFT. (h) Binding energies between LiPS species and $C_2N$ or Co-SAs/$C_2N$ as calculated by DFT.**

within Co-SAs/$C_2N$ was ∼2.2 (Table S3). Thus, on average, each Co atom is coordinated with two N atoms to form the Co−$N_2$ sites. The atomic structure model of Co-SAs/$C_2N$ is displayed as an inset in Figure 2c. The oscillation curve of Co-SAs/$C_2N$ is clearly distinct from that of CoPc and Co foil, again suggesting coordination of Co to N atoms (Figure 2d).

The wavelet transform (WT) of the Co K-edge spectrum was employed to further demonstrate the bonding environment of the Co species (Figure 2e−g). Compared with CoPc and Co foil, one prominent intensity maximum can be found at around 4.68 $Å^{-1}$, which belongs to the Co−N scattering path in the Co-SAs/$C_2N$ WT contour plot without observable Co−Co contribution.[36] This result further confirms the particular Co−N coordination environment at Co sites as well as the single-atom configurations in Co-SAs/$C_2N$. The atomic structure model of Co-SAs/$C_2N$ is displayed in Figure 2h.

The solid-state $^{13}C$ magic-angle-spinning (MAS) nuclear magnetic resonance (NMR) spectrum of Co-SAs/$C_2N$ is shown in Figure 2i. The resonance signal of Co-SAs/$C_2N$ is centered at around 150 ppm with a very broad distribution, indicating the carbon atoms of the phenyl edges connected to C=C units and the carbon atoms of triphenylene cores on vertices with intensive rigidity.[12] Besides, the continuous wave electron paramagnetic resonance (CW-EPR) signal at a *g*-value of 2.004 confirmed the presence of abundant defects with unpaired electrons in Co-SAs/$C_2N$ (Figure 2j).

For a deeper exploration of the electronic structure of Co-SAs/$C_2N$, DFT calculations were performed. As shown in Figure S5, the electronic band structure of Co-SAs/$C_2N$ obtained from the DFT calculations within the HSE06 functional showed several bands crossing the Fermi level, demonstrating that cobalt atom doping could improve the intrinsic conductivity of the $C_2N$ matrix.[12,37] The high electrical conductivity of Co-SAs/$C_2N$ was experimentally demonstrated using four-point electrical conductivity measurements (Figure S6).

To analyze the electrochemical performance of Co-SAs/$C_2N$ as a sulfur host in LSBs, sulfur was introduced within the Co-SAs/$C_2N$ by a melt-diffusion process.[38] SEM-EDX characterization, XRD patterns, thermogravimetric analysis (TGA), and the Brunauer−Emmett−Teller (BET) specific surface area of the obtained S@Co-SAs/$C_2N$ composites overall confirmed that sulfur was incorporated into the Co-SAs/$C_2N$ catalytic host (Figures S7−S10).

To evaluate the LiPS adsorption ability of the host material, certain amounts of Co-SAs/$C_2N$ and $C_2N$ were immersed in separate vials containing the same $1 \times 10^{-2}$ M $Li_2S_4$ solution. After overnight adsorption, the color of the $Li_2S_4$ solution containing Co-SAs/$C_2N$ was much lighter than that of the solution containing $C_2N$ (light yellow), indicating that the former has a much higher LiPS adsorption ability. This result was further confirmed using UV−vis spectroscopy (Figure 3a).[18,39]

Figure 3b shows the N 1s XPS spectrum of Co-SAs/$C_2N$ to red-shift after $Li_2S_4$ adsorption, which is related to a higher electronic density associated with the binding of the N atoms in $C_2N$, having a Lewis base character, and with Li atoms in $Li_2S_4$, having a Lewis acid character.[40−42] The formation of


https://doi.org/10.1021/acsenergylett.4c00771
ACS Energy Lett. 2024, 9, 2083−2091

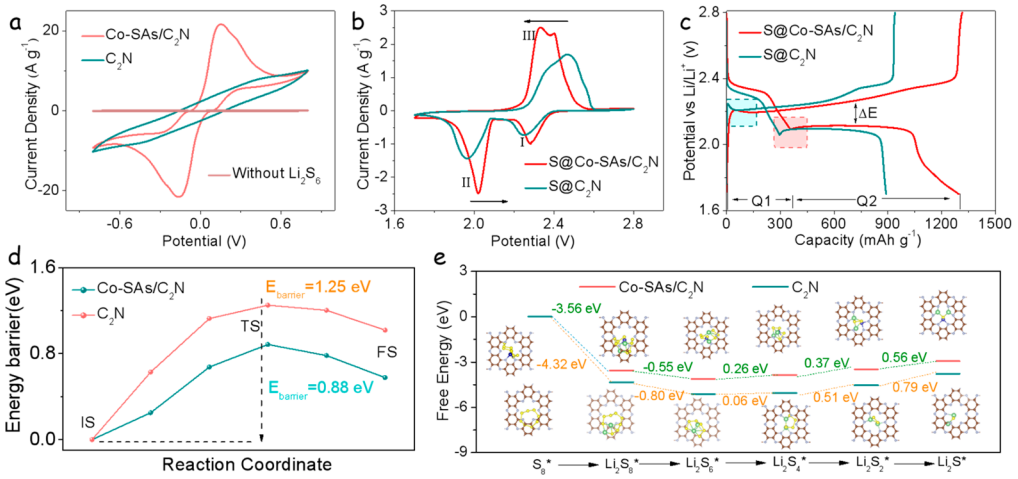


**Figure 4. (a) CV profiles of symmetric cells with Co-SAs/$C_2N$ and $C_2N$. (b) CV profiles of Li−S coin cells at a scan rate of 0.1 mV $s^{-1}$. (c) Charge/discharge profiles of various electrodes with a 0.1 C current rate. (d) Decomposition energy barriers of $Li_2S$ on $C_2N$ and Co-SAs/$C_2N$. (e) Gibbs free energy profiles of LiPS species on the surface of $C_2N$ and Co-SAs/$C_2N$.**

Li−N bonds was also confirmed by analyzing the Li 1s spectrum (Figure S11a). Figure 3c exhibits the high-resolution Co 3d XPS spectrum of Co-SAs/$C_2N$ to blue-shift after $Li_2S_4$ adsorption, which is likely due to the chemical interaction between Co and S, forming Co−S bonds.[27,43] In addition, the formation of Co−S bonds was also confirmed by analyzing the S 2p XPS spectrum of Co-SAs/$C_2N$−$Li_2S_4$ (Figure S11b).

To further study the interactions between Co-SAs/$C_2N$ and polysulfides, the $^7$Li NMR spectra of $Li_2S_4$ before and after interacting with Co-SAs/$C_2N$ were collected and displayed in Figure 3d,e. Because the chemical shift is quite sensitive to the surrounding environment, the changed chemical shift thus concurrently corresponds to the strong binding between $Li_2S_4$ and Co-SAs/$C_2N$. The pure $Li_2S_4$ shows a single peak at 0 ppm with a sharp signal, which becomes broader when attached to Co-SAs/$C_2N$. An additional broad signal appears at around −5 ppm, which is possibly due to the strong shielding effect caused by the Co-SAs/$C_2N$ rings. According to the above analysis and $^7$Li NMR experiments on the Co-SAs/$C_2N$−$Li_2S_4$ model system, a series of insights can be subtracted: (1) Co-SAs/$C_2N$ has strong binding to $Li_2S_4$ as suggested by the high binding energy; (2) a dipole−dipole interaction, namely a Li bond, forms between $Li_2S_4$ and Co-SAs/$C_2N$ to afford the strong binding; (3) the formation of a Li−N bond alters the local environment surrounding Li, resulting in a shift in the NMR spectrum.

The interactions between $Li_2S_4$ and Co-SAs/$C_2N$ were further confirmed by CW-EPR characterization. As shown in Figure 3f, a decrease in EPR signal intensity was obtained with $Li_2S_4$ adsorption. This lower EPR signal denotes a decrease in the density of unpaired electrons, which implies that the sites with unpaired electrons, e.g., carbon vacancies, serve as active sites for the adsorption of LiPS.

DFT calculations were performed to further evaluate the interaction between LiPS and Co-SAs/$C_2N$ (Figures S12 and S13). As shown in Figure 3g, the calculated binding energies ($E_b$) of $Li_2S_4$ on $C_2N$ and Co-SAs/$C_2N$ surfaces were −2.49 and −6.61 eV, respectively, which endows Co−$N_2$ sites with enhanced adsorption ability for $Li_2S_4$.[12,44] Actually, all the LiPS species showed a higher affinity for the Co-SAs/$C_2N$ surface rather than for the $C_2N$ one (Figure 3h). These results suggest robust chemisorption of LiPS on Co-SAs/$C_2N$, which should block the LiPS shuttle effect.

To reveal the electrocatalytic activity of Co-SAs/$C_2N$ for polysulfide conversion, CV measurements were initially performed on symmetric cells containing a $Li_2S_6$ electrolyte within a voltage window of −0.8 to 0.8 V (Figures 4a and S14). The Co-SAs/$C_2N$-based cell displayed two symmetric cathodic/anodic peaks, which were associated with the electrochemical oxidation/reduction of $Li_2S_6$:[45,46]

$$S_6^{2-} + 10e^- + 12Li^+ \leftrightarrow 6Li_2S \quad (1)$$

$$4S_6^{2-} \leftrightarrow 8e^- + 3S_8 \quad (2)$$

The cell containing Co-SAs/$C_2N$ electrodes provided higher currents compared with the $C_2N$-based cell, indicating the superior catalytic activity of Co-SAs/$C_2N$ toward the liquid−solid redox reaction ($Li_2S \leftrightarrow S_6^{2-} \leftrightarrow S_8$).

The CV curves of Li−S coin cells based on S@Co-SAs/$C_2N$ and S@C2N cathodes are shown in Figure 4b. The cathodic peak voltage (peak I) is associated with the reactions:[12,47]

$$S_8 + 2e^- + 2Li^+ \rightarrow Li_2S_8$$

$$3Li_2S_8 + 2e^- + 2Li^+ \rightarrow 4Li_2S_6$$

$$2Li_2S_6 + 2e^- + 2Li^+ \rightarrow 3Li_2S_4$$

The cathodic peak (peak II) corresponded to the reactions:

$$Li_2S_4 + 2e^- + 2Li^+ \rightarrow 2Li_2S_2$$

$$Li_2S_2 + 2e^- + 2Li^+ \rightarrow 2Li_2S$$

The anodic peak (peak III) accounts for the reverse multistep oxidation process of short-chain sulfides to LiPS and eventually to S.[48,49] S@Co-SAs/$C_2N$ electrodes exhibited much higher peak currents, and the cathodic/anodic peaks were located at more positive/negative potentials than S@$C_2N$, demonstrating that Co-SAs/$C_2N$ was the most effective catalyst in promoting the polysulfide redox reaction kinetics (Figures 4b, S15, and S16). At the different scan rates tested, S@Co-SAs/$C_2N$-based cells displayed higher redox peak currents. lower polarization potentials, and improved stability compared with those of S@$C_2N$-based cells (Figures S17 and


https://doi.org/10.1021/acsenergylett.4c00771
ACS Energy Lett. 2024, 9, 2083−2091

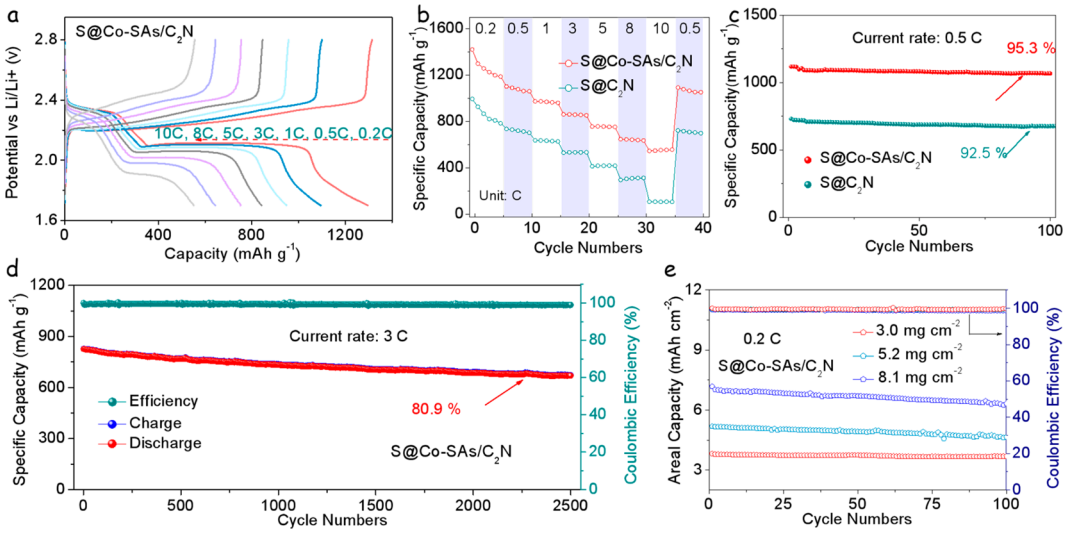


**Figure 5. (a) Charge/discharge profile of S@Co-SAs/$C_2N$ electrodes at various rates. (b) Rate capabilities and (c) capacity retention of S@Co-SAs/$C_2N$ and S@$C_2N$ electrodes. (d) Ultralong cycling test of the S@Co-SAs/$C_2N$ electrode at 3 C over 2500 cycles. (h) High-loading cycling performances with sulfur loadings of 3.0, 5.2, and 8.1 mg cm$^{-2}$ at 0.2 C of S@Co-SAs/$C_2N$ electrodes.**

S18). As shown in Figure S19, the cathodic/anodic peak currents showed a linear relationship with the square root of the scanning rates, pointing to a diffusion-limited reaction.[50,51] DFT calculations revealed this higher $Li^+$ diffusivity to be related to the decrease of the lithium-ion diffusion barrier on the $C_2N$ surface by the introduction of cobalt atoms (Figure S19e).

The galvanostatic charge−discharge profiles for S@Co-SAs/$C_2N$ and S@$C_2N$ electrodes at a current rate of 0.1 C are displayed in Figure 4c. S@Co-SAs/$C_2N$ electrodes were characterized by significantly lower polarization potentials ($\Delta E$ = 126 mV) and a higher Q2/Q1 ratio (2.62) than S@$C_2N$ electrodes ($\Delta E$ = 168 mV, Q2/Q1 = 1.99), confirming the superior catalytic activity of Co-SAs/$C_2N$ toward LiPS conversion (Figure S20).

Electrochemical kinetics was further assessed in the phase conversion between soluble LiPS and insoluble $Li_2S_2$/$Li_2S$ during the charge/discharge processes (Figures S21 and S22). Based on Faraday's law and the potentiostatic discharge profiles in Figure S22, S@Co-SAs/$C_2N$ electrodes showed faster responsivity toward $Li_2S$ nucleation and a higher capacity of $Li_2S$ precipitation (283.6 mA h g$^{-1}$) than S@$C_2N$ electrodes (192.1 mA h g$^{-1}$). This result further proved that Co-SAs/$C_2N$ with unsaturated Co−$N_2$ active sites significantly reduces the energy barrier of the $Li_2S$ nucleation, enhancing the $Li_2S$ precipitation kinetics.[16,52]

DFT calculations were further used to evaluate the reaction kinetics of the charging process on the surfaces of $C_2N$ and Co-SAs/$C_2N$ (Figures S23 and S24). As shown in Figure 4d, the energy barrier of $Li_2S$ decomposition on Co-SAs/$C_2N$ is only 0.88 eV, much lower than that on $C_2N$ (1.25 eV). This result points to $Li_2S$ being much more easily oxidized into LiPS on the Co-SAs/$C_2N$ surface than on $C_2N$ during the battery charging process, leading to improved redox reversibility between $Li_2S$ and LiPS and enhanced S utilization.[10,53]

The relative Gibbs free energy evolution of the reaction process is shown in Figure 4e. $S_8$ reacts with two Li ions to first form $Li_2S_8$, followed by further reduction of $Li_2S_8$ to form $Li_2S_6$. While the initial steps are exothermic, the subsequent tranformations of LiPS to $Li_2S_2$ and then to $Li_2S$ have an endothermic nature.[34,54] Thus, the formation of $Li_2S_2$ and $Li_2S$ are the rate-limiting steps of the sulfur reduction process. The Gibbs free energies associated with the production of $Li_2S_2$ and $Li_2S$ on the surface of Co-SAs/$C_2N$ are 0.37 and 0.56 eV, respectively, well below those calculated on the $C_2N$ surface (0.51 and 0.79 eV).

The galvanostatic charge/discharge profiles of S@Co-SAs/$C_2N$ and S@$C_2N$ at different current rates are exhibited in Figures 5a and S25. Figure 5b shows the rate performances of the cells based on the two electrodes tested at current rates from 0.2 to 10 C. S@Co-SAs/$C_2N$ electrodes showed a lower polarization and were characterized by an ultrahigh initial discharge capacity of 1415 mA h g$^{-1}$ at 0.2 C, pointing toward optimized sulfur activity and utilization. Even at the highest current rate of 10 C, an average capacity of 556 mAh g$^{-1}$ was stabilized, well above the capacity obtained for the S@$C_2N$ electrodes.

Figure 5c displays the cycling tests of different cells based on S@Co-SAs/$C_2N$ and S@$C_2N$ cathodes at 0.5 C. S@Co-SAs/$C_2N$ electrodes delivered an initial discharge capacity of 1118.6 mAh g$^{-1}$ and maintained a stable capacity of 1066.2 mAh g$^{-1}$ after 100 cycles. For comparison, the discharge capacity of the S@$C_2N$ electrodes decayed to 676.5 mAh g$^{-1}$ after 100 cycles, with a capacity loss of 7.5%. Electrochemical impedance spectroscopy (EIS) was used to further understand the parameters behind the enhanced redox kinetics of the S@Co-SAs/$C_2N$ electrodes. The S@Co-SAs/$C_2N$ electrodes were characterized by considerably lower $R_p$ and $R_{ct}$ compared with S@$C_2N$ electrodes after cycling (Figure S26 and Table S4), indicating improved electrode kinetics. Besides, both electrodes displayed a decrease of the $R_{ct}$ once activated, which is in part related to an improved electrode architecture and electrolyte wetting.

Additional cycling tests were carried out on the S@Co-SAs/$C_2N$ electrodes at various current rates (Figures 5d and S27). The S@Co-SAs/$C_2N$ electrode provided an initial discharge capacity at 3 C of 826 mAh g$^{-1}$ and retained 80.9% of its capacity after 2500 cycles, indicating a low capacity decay rate of just 0.008% per cycle. In addition, as exhibited in Figure S28, S@Co-SAs/$C_2N$ electrodes displayed energy efficiencies


https://doi.org/10.1021/acsenergylett.4c00771
ACS Energy Lett. 2024, 9, 2083−2091

of around 92.1% at 0.2 C, well above that of S@$C_2N$ electrodes.

Figures 5e and S29 show the performance of the S@Co-SAs/$C_2N$ electrodes at a sulfur loading of 3.0, 5.2, and 8.1 mg $cm^{-2}$ at 0.2 C and an electrolyte-to-sulfur (E/S) ratio of 8.9, 6.1, and 4.7 $\mu$L $mg^{-1}$, respectively. High areal capacities of 3.69, 4.64, and 6.32 mAh $cm^{-2}$ after 100 cycles can be obtained under the sulfur loading of 3.0, 5.2, and 8.1 mg $cm^{-2}$, respectively. S@Co-SAs/$C_2N$ electrodes displayed stable charge/discharge curves and delivered a high areal capacity of 7.18 mAh $cm^{-2}$ under a sulfur loading of 8.1 mg $cm^{-2}$, which is almost a 2-fold of that of commercial Li-ion batteries (4 mAh $cm^{-2}$). This excellent performance at a high sulfur loading confirmed the good reaction kinetics, which is attributed to the superior catalytic activity of the unsaturated Co−$N_2$ sites of Co-SAs/$C_2N$.

Figure S30 shows SEM images of the S@Co-SAs/$C_2N$ cathodes with a high S loading after cycling, showing no cracks. From the EDS spectrum of the Li anode after cycling, only a very small amount of sulfur was observed, proving the inhibition of LiPS migration (Figure S31). To further demonstrate the important role played by Co in the superior material performance, additional samples with a lower Co amount were produced and tested. As expected, the performance of this sample was sensibly lower than that of the sample containing a higher amount of Co but improved with respect to the sample containing no Co (Figure S32). The electrochemical results of S@Co-SAs/$C_2N$ cathodes for LSBs are compared to other state-of-the-art single-atom-based materials in Table S5 (Supporting Information). Besides, to demonstrate the potential for practical use of S@Co-SAs/$C_2N$ cathodes, we scaled them up to pouch cell level reaching a capacity of 725 mAh $g^{-1}$ at 0.35 C (Figure S33).

In summary, the synthesis of Co-SAs/$C_2N$ with a precise Co−$N_2$ coordination structure and its use to explore the adsorption and catalytic properties of Co−$N_2$ sites in the conversion process of LiPS have been described. Co-SAs/$C_2N$ exhibits lithiophilic/sulfiphilic binding with polysulfides to prevent the dissolution of LiPS in the electrolyte. Besides, within this structure, the unsaturated Co−$N_2$ center can act as a multifunctional site for accelerating the redox conversion of LiPS and reducing the reaction energy barrier of $Li_2S$ deposition and decomposition during discharge/charge processes, as determined by X-ray absorption fine spectroscopy, experiments, and DFT calculations. As a result, S@Co-SAs/$C_2N$ cathodes deliver excellent rate performance and ultra-long-term cycling stability. Even at high sulfur loadings and under lean electrolyte conditions, S@Co-SAs/$C_2N$ cathodes display a remarkable areal capacity meeting the demands of commercial LIBs. This work sheds light on the dual adsorption-catalysis effect of Co-SAs/$C_2N$ with an unsaturated coordination structure (Co−$N_2$ sites) for the redox conversion of LiPS, providing new insights for designing SAC-based hosts with maximized activity in improving the performance of LSBs.

## ■ ASSOCIATED CONTENT

### Supporting Information

The Supporting Information is available free of charge at https://pubs.acs.org/doi/10.1021/acsenergylett.4c00771.

Figures S1−S28 and Tables S1−S5 as described in the text, specifically, additional HAADF-STEM, XANES, XRD, XPS, TGA, CV, electrochemical performance, DFT simulation results, and crystal structure (PDF)

## ■ AUTHOR INFORMATION


### Corresponding Authors

**Ming Xu** − *State Key Laboratory of Chemical Resource Engineering, Beijing University of Chemical Technology, Beijing 100029, P. R. China*; Email: mingxu@mail.buct.edu.cn

**David Mitlin** − *Materials Science and Engineering Program & Texas Materials Institute, The University of Texas at Austin, Austin, Texas 78712, United States*; Email: david.mitlin2@utexas.edu

**Guangmin Zhou** − *Shenzhen Geim Graphene Center, Tsinghua-Berkeley Shenzhen Institute & Tsinghua Shenzhen, International Graduate School, Tsinghua University, Shenzhen 518055, P. R. China*; orcid.org/0000-0002-3629-5686; Email: guangminzhou@sz.tsinghua.edu.cn

**Andreu Cabot** − *Catalonia Institute for Energy Research − IREC, Sant Adrià de Besòs, Barcelona 08930, Spain; ICREA, 08010 Barcelona, Spain*; orcid.org/0000-0002-7533-3251; Email: acabot@irec.cat

### Authors

**Dawei Yang** − *Henan Province Key Laboratory of Photovoltaic Materials, School of Future Technology, Henan University, Kaifeng 475004, P. R. China; Catalonia Institute for Energy Research − IREC, Sant Adrià de Besòs, Barcelona 08930, Spain*; orcid.org/0000-0002-3842-8286

**Jiaao Wang** − *Department of Chemistry and the Oden Institute for Computational Engineering and Sciences, The University of Texas at Austin, Austin, Texas 78712, United States*; orcid.org/0000-0002-4944-4951

**Chenjie Lou** − *Center for High Pressure Science and Technology Advanced Research, Beijing 100193, P. R. China*

**Mengyao Li** − *School of Physics and Microelectronics, Zhengzhou University, Zhengzhou 450052, P. R. China*; orcid.org/0000-0002-9082-7938

**Chaoqi Zhang** − *Catalonia Institute for Energy Research − IREC, Sant Adrià de Besòs, Barcelona 08930, Spain*

**Alberto Ramon** − *Catalonia Institute for Energy Research − IREC, Sant Adrià de Besòs, Barcelona 08930, Spain*

**Canhuang Li** − *Catalonia Institute for Energy Research − IREC, Sant Adrià de Besòs, Barcelona 08930, Spain*

**Mingxue Tang** − *Center for High Pressure Science and Technology Advanced Research, Beijing 100193, P. R. China*; orcid.org/0000-0002-7282-4100

**Graeme Henkelman** − *Department of Chemistry and the Oden Institute for Computational Engineering and Sciences, The University of Texas at Austin, Austin, Texas 78712, United States*; orcid.org/0000-0002-0336-7153

**Junshan Li** − *Institute for Advanced Study, Chengdu University, 610106 Chengdu, P. R. China*; orcid.org/0000-0002-1482-1972

**Jordi Llorca** − *Institute of Energy Technologies, Department of Chemical Engineering and Barcelona Research Center in Multiscale Science and Engineering, Universitat Politècnica de Catalunya, EEBE, 08019 Barcelona, Spain*; orcid.org/0000-0002-7447-9582

**Jordi Arbiol** − *Catalan Institute of Nanoscience and Nanotechnology (ICN2), Bellaterra 08193 Barcelona, Spain*; orcid.org/0000-0002-0695-1726




https://doi.org/10.1021/acsenergylett.4c00771
ACS Energy Lett. 2024, 9, 2083−2091

Complete contact information is available at:
https://pubs.acs.org/10.1021/acsenergylett.4c00771

### Notes

The authors declare no competing financial interest.

## ■ ACKNOWLEDGMENTS

This work was supported by MCIN/AEI/10.13039/501100011033/and by "ERDF A way of making Europe", by the "European Union" through the projects ENE2016-77798-C4-3-R and PID2020-116093RB-C43. D. Yang thanks the China Scholarship Council for the scholarship support and the funding from the National Natural Science Foundation of China (NSFC) (Grants No. 22305064). M. Tang and M. Xu thank the financial support by the National Natural Science Foundation of China (Grants 21974007, U1930401, and 22102007). ICN2 acknowledges the support from the Severo Ochoa Programme from Spanish MCIN/AEI (Grant No.: CEX2021-001214-S) and Generalitat de Catalunya 2021SGR00457. This study is part of the Advanced Materials programme and was supported by MCIN with funding from European Union NextGenerationEU (PRTR-C17.I1) and by Generalitat de Catalunya. IREC and ICN2 are both funded by the CERCA Programme/Generalitat de Catalunya. This work was supported by Fundamental Research Funds for the Central Universities (buctrc202112). J. Llorca is a Serra Húnter Fellow and is grateful to projects PID2021-124572OB-C31 and GC2021 SGR 01061 and to ICREA Academia program. This project has received funding from the European Union's Horizon 2020 research and innovation programme under grant agreement No 823717-ESTEEM3. Part of the present work has been performed in the framework of Universitat Autònoma de Barcelona Materials Science PhD program. The authors are thankful for the support of the BSRF (Beijing Synchrotron Radiation Facility) during the XAFS measurements at the beamline 1W1B, 4B7A, 4B7B, 4B9B, and Shanghai Synchrotron Radiation Facility (SSRF).

## ■ REFERENCES

(1) Bruce, P. G.; Freunberger, S. A.; Hardwick, L. J.; Tarascon, J. M. $LigO_2$ and LigS Batteries with High Energy Storage. *Nat. Mater.* **2012**, *11* (1), 19−29.

(2) Zhou, G.; Wang, D. W.; Li, F.; Hou, P. X.; Yin, L.; Liu, C.; Lu, G. Q.; Gentle, I. R.; Cheng, H. M. A Flexible Nanostructured Sulphur-Carbon Nanotube Cathode with High Rate Performance for Li-S Batteries. *Energy Environ. Sci.* **2012**, *5* (10), 8901−8906.

(3) Li, Z.; Guan, B. Y.; Zhang, J.; Lou, X. W. A Compact Nanoconfined Sulfur Cathode for High-Performance Lithium-Sulfur Batteries. *Joule* **2017**, *1* (3), 576−587.

(4) Zhao, C.; Jiang, B.; Huang, Y.; Sun, X.; Wang, M.; Zhang, Y.; Zhang, N. Highly active and stable oxygen vacancies via sulfur modification for efficient catalysis in lithium-sulfur batteries. *Energy Environ. Sci.* **2023**, *16* (10), 5490−5499.

(5) Chen, X.; Peng, H. J.; Zhang, R.; Hou, T. Z.; Huang, J. Q.; Li, B.; Zhang, Q. An Analogous Periodic Law for Strong Anchoring of Polysulfides on Polar Hosts in Lithium Sulfur Batteries: S- or Li-Binding on First-Row Transition-Metal Sulfides? *ACS Energy Lett.* **2017**, *2* (4), 795−801.

(6) Yang, Y.; Zheng, G.; Cui, Y. Nanostructured Sulfur Cathodes. *Chem. Soc. Rev.* **2013**, *42* (7), 3018−3032.

(7) He, J.; Luo, L.; Chen, Y.; Manthiram, A. Yolk-Shelled C@$Fe_3O_4$ Nanoboxes as Efficient Sulfur Hosts for High-Performance Lithium-Sulfur Batteries. *Adv. Mater.* **2017**, *29* (34), 1702707.

(8) Sun, Z.; Zhang, J.; Yin, L.; Hu, G.; Fang, R.; Cheng, H. M.; Li, F. Conductive Porous Vanadium Nitride/Graphene Composite as Chemical Anchor of Polysulfides for Lithium-Sulfur Batteries. *Nat. Commun.* **2017**, *8*, 14627.

(9) Li, G.; Lei, W.; Luo, D.; Deng, Y.; Deng, Z.; Wang, D.; Yu, A.; Chen, Z. Stringed "Tube on Cube" Nanohybrids as Compact Cathode Matrix for High-Loading and Lean-Electrolyte Lithium-Sulfur Batteries. *Energy Environ. Sci.* **2018**, *11* (9), 2372−2381.

(10) Zhang, L.; Liu, D.; Muhammad, Z.; Wan, F.; Xie, W.; Wang, Y.; Song, L.; Niu, Z.; Chen, J. Single Nickel Atoms on Nitrogen-Doped Graphene Enabling Enhanced Kinetics of Lithium-Sulfur Batteries. *Adv. Mater.* **2019**, *31* (40), 1903955.

(11) Liu, J.; Yuan, L.; Yuan, K.; Li, Z.; Hao, Z.; Xiang, J.; Huang, Y. SnO2 as a high-efficiency polysulfide trap in lithium-sulfur batteries. *Nanoscale.* **2016**, *8* (28), 13638.

(12) Yang, D.; Liang, Z.; Zhang, C.; Biendicho, J. J.; Botifoll, M.; Spadaro, M. C.; Chen, Q.; Li, M.; Ramon, A.; Moghaddam, A. O.; Llorca, J.; Wang, J.; Morante, J. R.; Arbiol, J.; Chou, S. L.; Cabot, A. $NbSe_2$ Meets $C_2N$: A 2D-2D Heterostructure Catalysts as Multifunctional Polysulfide Mediator in Ultra-Long-Life Lithium-Sulfur Batteries. *Adv. Energy Mater.* **2021**, *11* (36), 2101250.

(13) Wang, M.; Fan, L.; Sun, X.; Guan, B.; Jiang, B.; Wu, X.; Tian, D.; Sun, K.; Qiu, Y.; Yin, X.; Zhang, Y.; Zhang, N. Nitrogen-Doped $CoSe_2$ as a Bifunctional Catalyst for High Areal Capacity and Lean Electrolyte of Li-S Battery. *ACS Energy Lett.* **2020**, *5* (9), 3041−3050.

(14) Sun, X.; Qiu, Y.; Jiang, B.; Chen, Z.; Zhao, C.; Zhou, H.; Yang, L.; Fan, L.; Zhang, Y.; Zhang, N. Isolated Fe-Co heteronuclear diatomic sites as efficient bifunctional catalysts for high-performance lithium-sulfur batteries. *Nat. Commun.* **2023**, *14* (1), 291.

(15) Zhang, Y.; Liu, J.; Wang, J.; Zhao, Y.; Luo, D.; Yu, A.; Wang, X.; Chen, Z. Engineering Oversaturated Fe-N 5 Multifunctional Catalytic Sites for Durable Lithium-Sulfur Batteries. *Angew. Chem., Int. Ed.* **2021**, *133* (51), 26826−26833.

(16) Zhang, X.; Yang, T.; Zhang, Y.; Wang, X.; Wang, J.; Li, Y.; Yu, A.; Wang, X.; Chen, Z. Single Zinc Atom Aggregates: Synergetic Interaction to Boost Fast Polysulfide Conversion in Lithium-Sulfur Batteries. *Adv. Mater.* **2023**, *35* (6), 2208470.

(17) Wang, J.; Qiu, W.; Li, G.; Liu, J.; Luo, D.; Zhang, Y.; Zhao, Y.; Zhou, G.; Shui, L.; Wang, X.; Chen, Z. Coordinatively Deficient Single-Atom Fe-N-C Electrocatalyst with Optimized Electronic Structure for High-Performance Lithium-Sulfur Batteries. *Energy Storage Mater.* **2022**, *46*, 269−277.

(18) Han, Z.; Zhao, S.; Xiao, J.; Zhong, X.; Sheng, J.; Lv, W.; Zhang, Q.; Zhou, G.; Cheng, H. M. Engineering D-p Orbital Hybridization in Single-Atom Metal-Embedded Three-Dimensional Electrodes for Li-S Batteries. *Adv. Mater.* **2021**, *33* (44), 2105947.

(19) Qiu, Y.; Fan, L.; Wang, M.; Yin, X.; Wu, X.; Sun, X.; Tian, D.; Guan, B.; Tang, D.; Zhang, N. Precise Synthesis of Fe-$N_2$ sites with High Activity and Stability for Long-Life Lithium-Sulfur Batteries. *ACS Nano* **2020**, *14* (11), 16105−16113.

(20) Fei, H.; Dong, J.; Feng, Y.; Allen, C. S.; Wan, C.; Volosskiy, B.; Li, M.; Zhao, Z.; Wang, Y.; Sun, H.; An, P.; Chen, W.; Guo, Z.; Lee, C.; Chen, D.; Shakir, I.; Liu, M.; Hu, T.; Li, Y.; Kirkland, A. I.; Duan, X.; Huang, Y. General Synthesis and Definitive Structural Identification of $MN_4C_4$ Single-Atom Catalysts with Tunable Electrocatalytic Activities. *Nat. Catal.* **2018**, *1* (1), 63−72.

(21) Zhang, Y.; Qiu, Y.; Fan, L.; Sun, X.; Jiang, B.; Wang, M.; Wu, X.; Tian, D.; Song, X.; Yin, X.; Shuai, Y.; Zhang, N. Dual-atoms iron sites boost the kinetics of reversible conversion of polysulfide for high-performance lithium-sulfur batteries. *Energy Storage Mater.* **2023**, *63*, 103026.

(22) Chen, K.; Liu, K.; An, P.; Li, H.; Lin, Y.; Hu, J.; Jia, C.; Fu, J.; Li, H.; Liu, H.; Lin, Z.; Li, W.; Li, J.; Lu, Y. R.; Chan, T. S.; Zhang, N.; Liu, M. Iron Phthalocyanine with Coordination Induced Electronic Localization to Boost Oxygen Reduction Reaction. *Nat. Commun.* **2020**, *11* (1), 4173.

(23) Ding, Y.; Cheng, Q.; Wu, J.; Yan, T.; Shi, Z.; Wang, M.; Yang, D.; Wang, P.; Zhang, L.; Sun, J. Enhanced Dual-Directional Sulfur Redox via a Biotemplated Single-Atomic Fe-$N_2$ Mediator Promises Durable Li-S Batteries. *Adv. Mater.* **2022**, *34* (28), 2202256.

(24) Zhong, W.; Qiu, Y.; Shen, H.; Wang, X.; Yuan, J.; Jia, C.; Bi, S.; Jiang, J. Electronic Spin Moment As a Catalytic Descriptor for Fe Single-Atom Catalysts Supported on $C_2N$. *J. Am. Chem. Soc.* **2021**, *143* (11), 4405−4413.
(25) Lin, C.; Zhang, H.; Song, X.; Kim, D. H.; Li, X.; Jiang, Z.; Lee, J. H. 2D-Organic Framework Confined Metal Single Atoms with the Loading Reaching the Theoretical Limit. *Mater. Horizons* **2020**, *7* (10), 2726−2733.
(26) Xu, J.; Mahmood, J.; Dou, Y.; Dou, S.; Li, F.; Dai, L.; Baek, J. B. 2D Frameworks of $C_2N$ and $C_3N$ as New Anode Materials for Lithium-Ion Batteries. *Adv. Mater.* **2017**, *29* (34), 1702007.
(27) Liang, Z.; Yang, D.; Tang, P.; Zhang, C.; Jacas Biendicho, J.; Zhang, Y.; Llorca, J.; Wang, X.; Li, J.; Heggen, M.; David, J.; Dunin-Borkowski, R. E.; Zhou, Y.; Morante, J. R.; Cabot, A.; Arbiol, J. Atomically Dispersed Fe in a $C_2N$ Based Catalyst as a Sulfur Host for Efficient Lithium-Sulfur Batteries. *Adv. Energy Mater.* **2021**, *11* (5), 2003507.
(28) Chu, C.; Zhu, Q.; Pan, Z.; Gupta, S.; Huang, D.; Du, Y.; Weon, S.; Wu, Y.; Muhich, C.; Stavitski, E.; Domen, K.; Kim, J. H. Spatially Separating Redox Centers on 2D Carbon Nitride with Cobalt Single Atom for Photocatalytic $H_2O_2$ Production. *Proc. Natl. Acad. Sci. U.S.A.* **2020**, *117* (12), 6376−6382.
(29) Shen, T.; Huang, X.; Xi, S.; Li, W.; Sun, S.; Hou, Y. The ORR Electron Transfer Kinetics Control via Co-$N_x$ and Graphitic N Sites in Cobalt Single Atom Catalysts in Alkaline and Acidic Media. *J. Energy Chem.* **2022**, *68*, 184−194.
(30) Lu, Q.; Wu, H.; Zheng, X.; Chen, Y.; Rogach, A. L.; Han, X.; Deng, Y.; Hu, W. Encapsulating Cobalt Nanoparticles in Interconnected N-Doped Hollow Carbon Nanofibers with Enriched Co-N-C Moiety for Enhanced Oxygen Electrocatalysis in Zn-Air Batteries. *Adv. Sci.* **2021**, *8* (20), 2101438.
(31) Pei, Z.; Lu, X. F.; Zhang, H.; Li, Y.; Luan, D.; Lou, X. W. Highly Efficient Electrocatalytic Oxygen Evolution Over Atomically Dispersed Synergistic Ni/Co Dual Sites. *Angew. Chem., Int. Ed.* **2022**, *134* (40), No. e202207537.
(32) Yao, Y.; Huang, Z.; Xie, P.; Wu, L.; Ma, L.; Li, T.; Pang, Z.; Jiao, M.; Liang, Z.; Gao, J.; He, Y.; Kline, D. J.; Zachariah, M. R.; Wang, C.; Lu, J.; Wu, T.; Li, T.; Wang, C.; Shahbazian-Yassar, R.; Hu, L. High temperature shockwave stabilized single atoms. *Nat. Nanotechnol.* **2019**, *14*, 851−857.
(33) Ding, K.; Hu, J.; Luo, J.; Zhao, L.; Jin, W.; Liu, Y.; Wu, Z.; Zou, G.; Hou, H.; Ji, X. Robust Electronic Correlation of Co-$CoN_4$ Hybrid Active Sites for Durable Rechargeable Zn-Air Batteries. *Adv. Funct. Mater.* **2022**, *32* (52), 2207331.
(34) Du, Z.; Chen, X.; Hu, W.; Chuang, C.; Xie, S.; Hu, A.; Yan, W.; Kong, X.; Wu, X.; Ji, H.; Wan, L. J. Cobalt in Nitrogen-Doped Graphene as Single-Atom Catalyst for High-Sulfur Content Lithium-Sulfur Batteries. *J. Am. Chem. Soc.* **2019**, *141* (9), 3977−3985.
(35) Shi, W.; Li, Z.; Gong, Z.; Liang, Z.; Liu, H.; Han, Y. C.; Niu, H.; Song, B.; Chi, X.; Zhou, J.; Wang, H.; Xia, B.; Yao, Y.; Tian, Z.-Q. Transient and general synthesis of high-density and ultrasmall nanoparticles on two-dimensional porous carbon via coordinated carbothermal shock. *Nat. Commun.* **2023**, *14*, 2294.
(36) Wang, Z.; Jin, X.; Zhu, C.; Liu, Y.; Tan, H.; Ku, R.; Zhang, Y.; Zhou, L.; Liu, Z.; Hwang, S. J.; Fan, H. J. Atomically Dispersed $Co_2$-$N_6$ and Fe-$N_4$ Costructures Boost Oxygen Reduction Reaction in Both Alkaline and Acidic Media. *Adv. Mater.* **2021**, *33* (49), 2104718.
(37) Wang, L.; Ni, Y.; Hou, X.; Chen, L.; Li, F.; Chen, J. A Two-Dimensional Metal-Organic Polymer Enabled by Robust Nickel-Nitrogen and Hydrogen Bonds for Exceptional Sodium-Ion Storage. *Angew. Chem., Int. Ed.* **2020**, *59* (49), 22126−22131.
(38) Yang, D.; Zhang, C.; Biendicho, J. J.; Han, X.; Liang, Z.; Du, R.; Li, M.; Li, J.; Arbiol, J.; Llorca, J.; Zhou, Y.; Morante, J. R.; Cabot, A. ZnSe/N-Doped Carbon Nanoreactor with Ultiple Adsorption Sites for Stable Lithium-Sulfur Batteries. *ACS Nano* **2020**, *14* (11), 15492−15504.
(39) Song, J.; Yu, Z.; Gordin, M. L.; Wang, D. Advanced Sulfur Cathode Enabled by Highly Crumpled Nitrogen Doped Graphene Sheets for High-Energy-Density Lithium-Sulfur Batteries. *Nano Lett.* **2016**, *16*, 864−870.
(40) Song, Y.; Zou, L.; Wei, C.; Zhou, Y.; Hu, Y. Single-Atom Electrocatalysts for Lithium-Sulfur Chemistry: Design Principle, Mechanism, and Outlook. *Carbon Energy* **2023**, *5*, No. e286.
(41) Liang, Z.; Shen, J.; Xu, X.; Li, F.; Liu, J.; Yuan, B.; Yu, Y.; Zhu, M. Advances in the Development of Single-Atom Catalysts for High-Energy-Density Lithium-Sulfur Batteries. *Adv. Mater.* **2022**, *34* (30), 2200102.
(42) Pang, Q.; Tang, J.; Huang, H.; Liang, X.; Hart, C.; Tam, K. C.; Nazar, L. F. A Nitrogen and Sulfur Dual-Doped Carbon Derived from Polyrhodanine@Cellulose for Advanced Lithium-Sulfur Batteries. *Adv. Mater.* **2015**, *27* (39), 6021−6028.
(43) Zhang, C.; Du, R.; Biendicho, J. J.; Yi, M.; Xiao, K.; Yang, D.; Zhang, T.; Wang, X.; Arbiol, J.; Llorca, J.; Zhou, Y.; Morante, J. R.; Cabot, A. Tubular CoFeP@CN as a Mott-Schottky Catalyst with Multiple Adsorption Sites for Robust Lithium-Sulfur Batteries. *Adv. Energy Mater.* **2021**, *11*, 2100432.
(44) Zheng, J.; Tian, J.; Wu, D.; Gu, M.; Xu, W.; Wang, C.; Gao, F.; Engelhard, M. H.; Zhang, J.-G.; Liu, J.; Xiao, J. Lewis Acid-Base Interactions between Polysulfides and Metal Organic Framework in Lithium Sulfur Batteries. *Nano Lett.* **2014**, *14*, 2345−2352.
(45) Zhou, G.; Yang, A.; Gao, G.; Yu, X.; Xu, J.; Liu, C.; Ye, Y.; Pei, A.; Wu, Y.; Peng, Y.; Li, Y.; Liang, Z.; Liu, K.; Wang, L.-W.; Cui, Y. Supercooled Liquid Sulfur Maintained in Three-Dimensional Current Collector for High-Performance Li-S Batteries. *Sci. Adv.* **2020**, *6* (21), No. eaay5098.
(46) Li, C.; Qi, S.; Zhu, L.; Zhao, Y.; Huang, R.; He, Y.; Ge, W.; Liu, X.; Zhao, M.; Xu, L.; Qian, Y. Regulating Polysulfide Intermediates by Ultrathin Co-Bi Nanosheet Electrocatalyst in Lithium-Sulfur Batteries. *Nano Today* **2021**, *40*, 101246.
(47) Lin, H.; Yang, L.; Jiang, X.; Li, G.; Zhang, T.; Yao, Q.; Zheng, G. W.; Lee, J. Y. Electrocatalysis of Polysulfide Conversion by Sulfur-Deficient $MoS_2$ Nanoflakes for Lithium-Sulfur Batteries. *Energy Environ. Sci.* **2017**, *10* (6), 1476−1486.
(48) Yang, D.; Liang, Z.; Tang, P.; Zhang, C.; Tang, M.; Li, Q.; Biendicho, J. J.; Li, J.; Heggen, M.; Dunin-Borkowski, R. E.; Xu, M.; Llorca, J.; Arbiol, J.; Morante, J. R.; Chou, S. L.; Cabot, A. A High Conductivity 1D $\pi$-d Conjugated Metal-Organic Framework with Efficient Polysulfide Trapping-Diffusion-Catalysis in Lithium-Sulfur Batteries. *Adv. Mater.* **2022**, *34* (10), 2108835.
(49) Moy, D.; Manivannan, A.; Narayanan, S. R. Direct Measurement of Polysulfide Shuttle Current: A Window into Understanding the Performance of Lithium-Sulfur Cells. *J. Electrochem. Soc.* **2015**, *162* (1), A1−A7.
(50) Chen, Y.; Zhang, W.; Zhou, D.; Tian, H.; Su, D.; Wang, C.; Stockdale, D.; Kang, F.; Li, B.; Wang, G. Co-Fe Mixed Metal Phosphide Nanocubes with Highly Interconnected-Pore Architecture as an Efficient Polysulfide Mediator for Lithium-Sulfur Batteries. *ASC nano* **2019**, *13*, 4731−4741.
(51) Yuan, Z.; Peng, H.; Hou, T.; Huang, J.; Chen, C.; Wang, D.; Cheng, X.; Wei, F.; Zhang, Q. Powering Lithium-Sulfur Battery Performance by Propelling Polysulfide Redox at Sulfiphilic Hosts. *Nano Lett.* **2016**, *16*, 519−527.
(52) Li, M.; Yang, D.; Biendicho, J. J.; Han, X.; Zhang, C.; Liu, K.; Diao, J.; Li, J.; Wang, J.; Heggen, M.; Dunin-Borkowski, R. E.; Wang, J.; Henkelman, G.; Morante, J. R.; Arbiol, J.; Chou, S. L.; Cabot, A. Enhanced Polysulfide Conversion with Highly Conductive and Electrocatalytic Iodine-Doped Bismuth Selenide Nanosheets in Lithium-Sulfur Batteries. *Adv. Funct. Mater.* **2022**, *32* (26), 2200529.
(53) Du, M.; Geng, P.; Pei, C.; Jiang, X.; Shan, Y.; Hu, W.; Ni, L.; Pang, H. High-Entropy Prussian Blue Analogues and Their Oxide Family as Sulfur Hosts for Lithium-Sulfur Batteries. *Angew. Chem., Int. Ed.* **2022**, *134* (41), No. e202209350.
(54) Xiao, R.; Yu, T.; Yang, S.; Chen, K.; Li, Z.; Liu, Z.; Hu, T.; Hu, G.; Li, J.; Cheng, H. M.; Sun, Z.; Li, F. Electronic Structure Adjustment of Lithium Sulfide by a Single-Atom Copper Catalyst toward High-Rate Lithium-Sulfur Batteries. *Energy Storage Mater.* **2022**, *51*, 890−899.


https://doi.org/10.1021/acsenergylett.4c00771
ACS Energy Lett. 2024, 9, 2083−2091